MAGNETOHYDRODYNAMICS Vol. 51 (2015), No. 3, pp. 461–471

# NUMERICAL AND EXPERIMENTAL INVESTIGATION OF THE CONTACTLESS INDUCTIVE FLOW TOMOGRAPHY IN THE PRESENCE OF STRONG STATIC MAGNETIC FIELDS

*M. Ratajczak, T. Wondrak, F. Stefani, S. Eckert*

*Helmholtz-Zentrum Dresden-Rossendorf e.V.,*
*P.O. Box 510119, 01314 Dresden, Germany*

In the continuous casting industry, electromagnetic brakes (EMBr) are used to influence the mould flow, although their effect on the flow cannot be directly examined due to a lack of market-ready measurement techniques for liquid metal flows. Contactless inductive flow tomography (CIFT) is a technique that is able to reconstruct the mean flow structure of an electrically conducting melt by measuring the flow-induced perturbations of an applied magnetic field outside the melt and solving the linear inverse problem. Since CIFT relies on the measurement of magnetic fields, the question arises: Does CIFT work in the presence of a strong static magnetic field like that of an EMBr that superimposes and distorts the applied excitation magnetic field? In this paper, we will examine the effects of EMBr on CIFT with simulations and accompanying measurements.

**Introduction.** More than 95% of the world's steel is produced every year by means of continuous casting [1]. In this technique, liquid metal flows from a tundish through a submerged entry nozzle (SEN) into a copper-walled mould (see Fig. 1). The mould is water-cooled so that a solid steel shell starts to form from the wall to the center of the mould. This strand with a still liquid core is then pulled out of the mould supported by rolls, where it solidifies completely, promoted by secondary cooling.

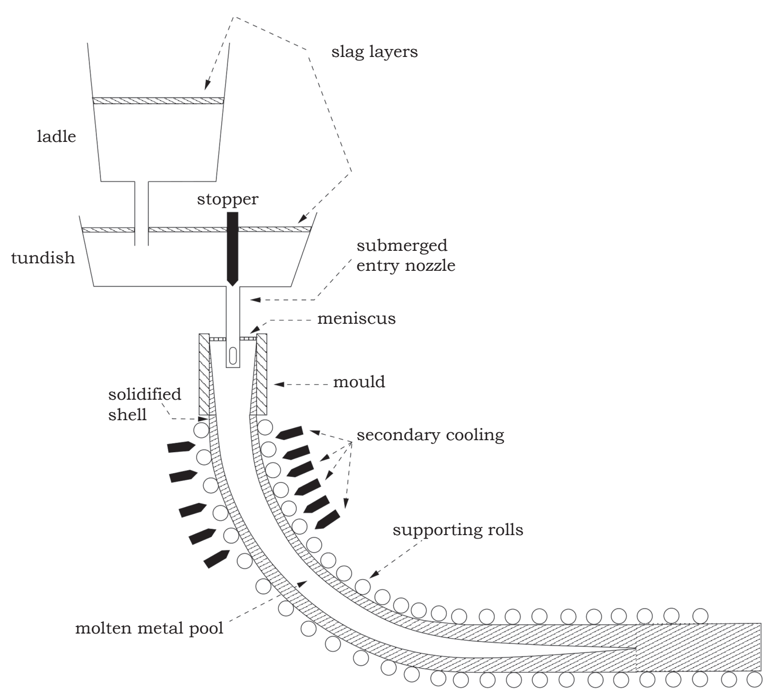


*Fig. 1.* Overview of the continuous casting process.

The quality of the resulting steel depends mostly on the flow structure in the mould [2]. For the casting of slabs, the so-called double-roll structure is desirable, where a liquid-metal jet leaves the SEN under some angle, impinges on the narrow face of the wall and then splits up into a small upper roll and a large lower roll. In contrast, an unstable flow with major oscillations can lead to several kinds of defects like longitudinal cracks or an uneven solidification shell [2]. In industry, electromagnetic brakes (EMBr) are used because it is assumed that a static magnetic field should create a stabilizing and decelerating effect on the jet. Although EMBrs have been used for almost 30 years, their braking effect could not be validated in detail due to a lack of measurement techniques.

The temperature and the opaqueness of the liquid steel make flow investigations in a real casting mould a challenging task for conventional measurement techniques. So far the industry uses techniques like the nail board dip test [3], the evaluation of oscillation mark shapes [3], the strain gauge method [4] and mould flow control sensors (MFC) from *AMEPA* [5]. Unfortunately, all these are mainly limited to measurements near the mould wall or near the meniscus (MFC, nail board) or suffer from very few measurement positions (strain gauge). A global contactless flow measurement technique would, therefore, be desirable.

The contactless inductive flow tomography (CIFT) achieves this by applying a magnetic field to the melt, measuring the flow-induced perturbations of the applied field and finally reconstructing the mean global flow from the measured field. In order to develop a flow measurement technique that can help resolving the open questions about the effects of EMBrs in continuous casting, the question arises: Does CIFT, relying on flow-induced magnetic field measurements of approx. 100 nT, still work in the presence of ferromagnetic components and static magnetic fields with a strength of more than 300 mT?

This paper is organized as follows: in section 1, we will give a short overview about the mathematical foundation of CIFT. Section 2 introduces the experimental setup before section 3 will show the simulation model and its validation. Finally, we will show the influence of a strong static magnetic field on CIFT in section 4.

**1. Theory.** We consider a fluid with electrical conductivity $\sigma$, relative permeability $\mu_r \approx 1$ (which is well justified for liquid steel) and velocity field $\mathbf{v}$ under the influence of a magnetic excitation field $\mathbf{B}_0$. Then, according to Ohm's law for moving conductors in the quasi-stationary approximation, we have

$$\mathbf{j} = \sigma(\mathbf{v} \times \mathbf{B} - \operatorname{grad}\varphi), \tag{1}$$

where $\mathbf{j}$ is the electric current density and $\varphi$ denotes the electric potential. Now $\mathbf{j}$ generates an additional magnetic field according to Biot–Savart's law

$$\begin{aligned} \mathbf{b}(\mathbf{r}) = & \frac{\mu_0\sigma}{4\pi} \iiint\limits_V \frac{(\mathbf{v}(\mathbf{r}') \times \mathbf{B}(\mathbf{r}')) \times (\mathbf{r} - \mathbf{r}')}{|\mathbf{r} - \mathbf{r}'|^3} \mathrm{d}V' \\ & - \frac{\mu_0\sigma}{4\pi} \oiint\limits_S \frac{\varphi(\mathbf{s}')\mathbf{n}(\mathbf{s}') \times (\mathbf{r} - \mathbf{s}')}{|\mathbf{r} - \mathbf{s}'|^3} \mathrm{d}S'. \end{aligned} \tag{2}$$

In this equation, $V$ and $S$ are the volume and the surface of the fluid, respectively, $\mu_0$ is the permeability of vacuum, $\mathbf{r}$ is a position in space and $\mathbf{n}$ denotes the normal vector at a position $\mathbf{s}$ on the surface $S$. Assuming divergence-free currents leads to the Poisson equation

$$\Delta\varphi = \boldsymbol{\nabla} \cdot (\mathbf{v} \times \mathbf{B}). \tag{3}$$

From this we derive the equation for the potential $\varphi$:

$$\begin{aligned}\varphi(\mathbf{s}) =& \frac{1}{2\pi} \iiint\limits_V \frac{(\mathbf{v}(\mathbf{r}') \times \mathbf{B}(\mathbf{r}')) \cdot (\mathbf{s} - \mathbf{r}')}{|\mathbf{s} - \mathbf{r}'|^3} \mathrm{d}V' \\ &- \frac{1}{2\pi} \oiint\limits_S \frac{\varphi(\mathbf{s}')\mathbf{n}(\mathbf{s}') \cdot (\mathbf{s} - \mathbf{s}')}{|\mathbf{s} - \mathbf{s}'|^3} \mathrm{d}S'.\end{aligned} \tag{4}$$

In general, the term $\mathbf{B}$ on the r. h. s. of these equations is the sum of the excitation field $\mathbf{B}_0$ and the flow induced magnetic field $\mathbf{b}$. For applications in, for example, continuous casting or in Czochralsky crystal growth, the magnetic Reynolds number $\mathrm{Rm} = \mu_0 \sigma v l$, where $v$ is a typical velocity scale and $l$ a typical length scale of the flow, is smaller than unity. In this case, we can neglect the contribution of $\mathbf{b}$ to $\mathbf{B}$ and, therefore, we can substitute $\mathbf{B}$ by $\mathbf{B}_0$.

The resulting linear inverse problem of inferring $\mathbf{v}$ from $\mathbf{b}$ is ill-posed because of its non-uniqueness [6]. Therefore, we need to apply a regularization method to our problem, which is in this case Tikhonov's regularization. We will not go into detail here and instead refer the reader to the publications [7, 8].

**2. Experimental setup.** Our goal is to develop a measurement technique for continuous casting. Continuous casting related experiments can be run at the Mini-LIMMCAST facility [9] that was established at the Helmholtz-Zentrum Dresden-Rossendorf, where cold liquid metal experiments can be conducted with hydrodynamically scaled models of real casting moulds. Mini-LIMMCAST mainly comprises a tundish, a mould and a catchment tank with the ternary eutectic alloy Gallium-Indium-Tin (GaInSn), which is liquid at room temperature [10] (see Fig. 2a,b). During the experiments, a stopper is lifted in the tundish, so the liquid metal flows through the mould into the catchment tank until the tundish is almost empty. Then the stopper is lowered and the GaInSn can be pumped up back into the tundish by means of an MHD pump. This discontinuous experimental mode limits the experimental time to roughly 50 sec, which is still sufficiently long to investigate the mould flow structures. The SEN and the mould can be exchanged easily in order to examine different casting configurations. The expected mould flow pattern is a double-roll flow structure, as sketched in Fig. 2a by the arrows [9].

The mould for our specific experiments was a downscaled model of a slab casting mould with a rectangular cross-section of $140 \times 35\,\mathrm{mm}^2$ and a height of 335 mm. The SEN had two oval-shaped outlets directed towards the narrow faces of the mould. The EMBr-system was of ruler-type, where the pole faces horizontally cover the wide face of the mould and are vertically aligned so that their upper edge coincides with the upper edge of the outlet ports of the SEN. The braking system, made of magnetically soft St37 type steel, created a magnetic flux perpendicular to the main flow direction with a maximum field strength of up to 310 mT at a DC electric current of $I_{\mathrm{EMBr}} = 200\,\mathrm{A}$. Exactly the same brake was used in experiments done by Timmel *et al.* in 2011 [11].

The excitation magnetic field $\mathbf{B}_0$ in the experiment was created by a rectangular coil around the mould just above the pole shoes. The coil current was generated by a power amplifier and a sine generator. The magnetic field mainly pointed towards the negative $z$-direction and had an amplitude in the order of 1 mT. The details will be given in section 4.

In past experiments, we used Fluxgate-sensors to measure the magnetic field [12–14]. While this sensor type has a great precision and is well-suited to determine induced magnetic fields less than 100 nT, it has an upper measurement range limit of 1.2 mT due to saturation effects. This makes them unusable for measurements

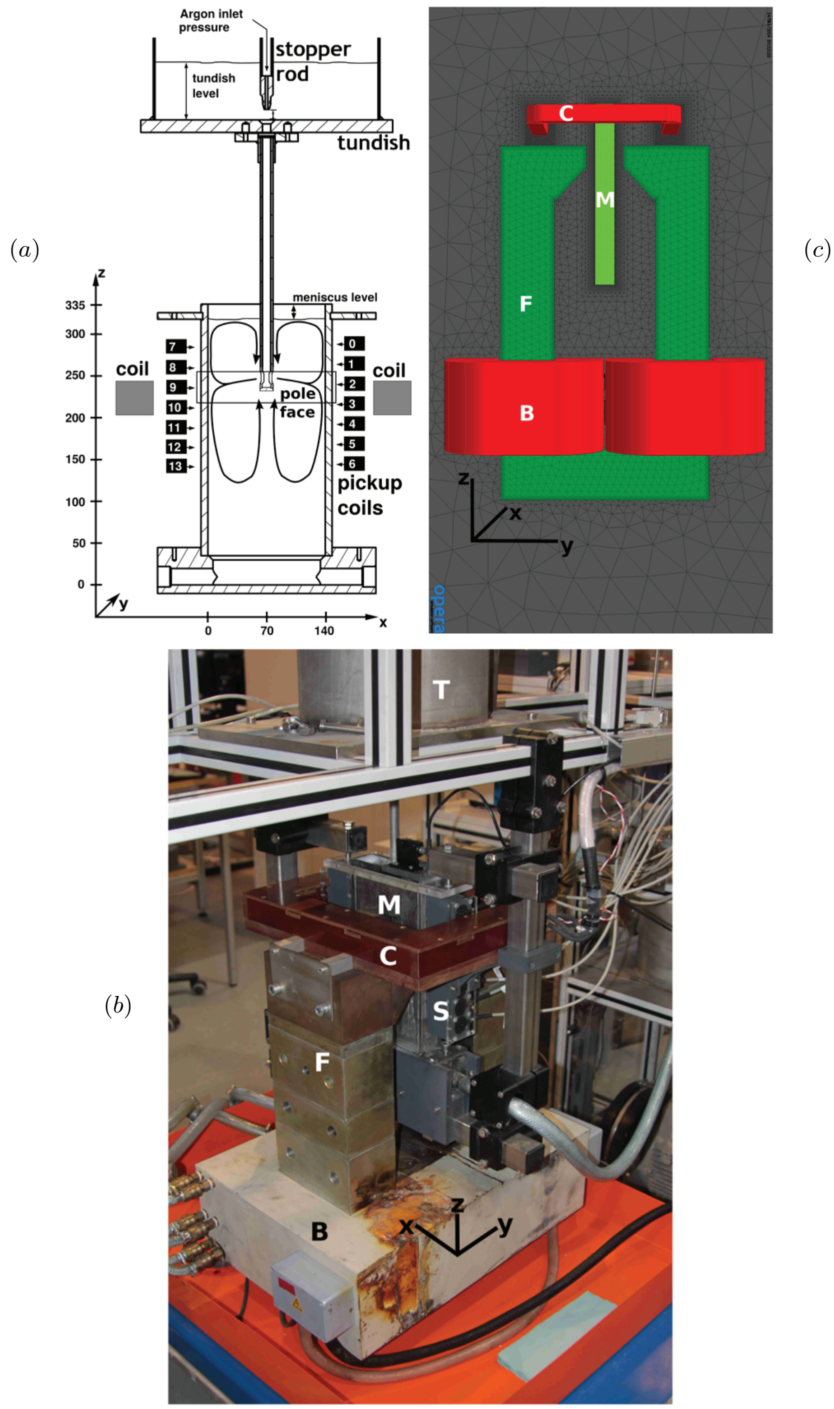


*Fig. 2.* Sketch (*a*) and photo (*b*) of the experimental setup; meshed simulation model (*c*). EMBr coils (B), excitation coil (C), fluxconductor (F), mould (M), sensor array containing the pickup-coils (S), tundish (T).

in the presence of a strong magnetic field like that of an EMBr. Therefore, we used induction-coil sensors (also called search coils or pickup coils), since these sensors have the advantages of no upper range limit, extreme linearity throughout a wide measurement range and immunity to static magnetic fields. This makes pickup coils robust against disturbing static magnetic fields from an EMBr because no voltage is induced. Obviously our excitation field $\mathbf{B}_0$ must be an AC magnetic field.

We designed two kinds of pickup coils: single coils, which pick up the absolute value of $\mathbf{B}$, and gradiometric coils, which detect the gradient of $\mathbf{B}$. The former have 340000 windings of a 25 µm wire wound around a cylinder with an outer diameter of 28 mm and a length of 29 mm, giving them a sensitivity of 510 V/(T Hz). The latter have two separate groups of windings with 160000 turns each, stacked on the central axis. The same wire type and outer measures were used for these coils, which gave us a sensitivity of 240 V/(T Hz). The sensors were distributed in groups of $2 \times 7$ along both narrow faces of the mould. We used this configuration in previous experiments [13] and simulations suggested that the highest amplitude of the induced magnetic field lay at this position. The signals picked up by the coils are differentially amplified by laboratory amplifiers made by FEMTO and then sampled by an AdWin 18-bit analog-digital-converter system with a time resolution of 1000 Hz. The sampled data is then processed with the Lomb-Scargle algorithm, following the implementation from Townsend [15], to determine the amplitude and the phase of the applied magnetic field and the in-phase component of the induced magnetic field.

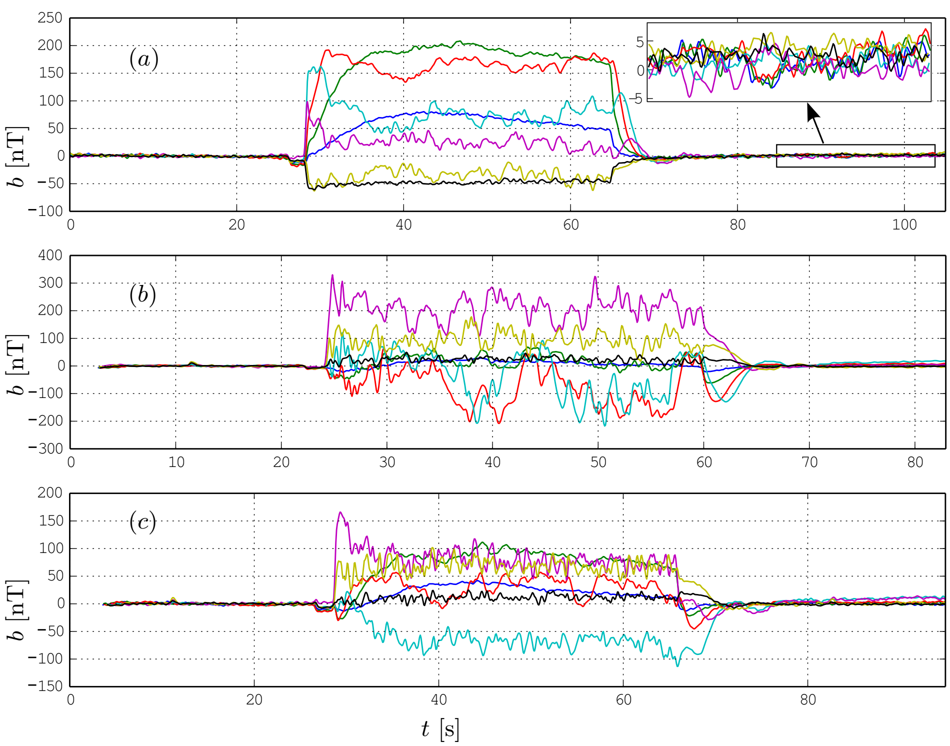


*Fig. 3.* Examples of the induced magnetic field $\mathbf{b}_x$ from different experiments, measured at 7 positions on one narrow face of the mould using gradiometric coils, for the cases of the brake switched off ($a$), the brake switched on (310 mT) with insulating mould walls ($b$) and the brake switched on with conducting mould walls ($c$). While the flow in ($a$) is very stable, ($b$) shows major fluctuations and ($c$) a stable but changed flow pattern compared with ($a$).

In order to investigate the signal quality of the induced magnetic field in the presence of the ferromagnetic parts and the static magnetic field from the EMBr, we did three experiments with the excitation frequency $f = 13$ Hz and 7 gradiometric coils on one narrow face of the mould. We show the results of those measurements in Fig. 3: the brake switched off ($a$) as a reference case, the brake switched on ($b$) with 310 mT and insulating mould walls, and the brake switched on with conducting walls ($c$). Whereas the reference case indicates a stable flow pattern, the flow becomes unstable if the magnetic field is switched on. If we change to conducting walls, the flow gets stable again, which was described also by Timmel *et al.* using UDV-measurements [11]. Note that we obtain a very clean signal in all three cases, as can be seen in the zoomed part of Fig. 3$a$.

**3. Simulation model.** In order to validate our measurements, we did accompanying simulations with the software suite Opera3D from Cobham. The simulation model, which was derived from the experimental setup, can be seen in Fig. 2$c$. The flux conductor was modelled as the magnetically soft type St37 steel with nonlinear isotropic permeability and electrical conductivity $\sigma_{\mathrm{St37}} = 2 \cdot 10^7$ S/m. We modelled the mould as a block of conductivity $\sigma_{\mathrm{GaInSn}} = 3.3 \cdot 10^6$ S/m.

In a first step, we compared our simulation of the brake field $\mathbf{B}_{\mathrm{EMBr}}$ with measurements. To get a rough knowledge of the spatial structure of the magnetic field from the EMBr; the amplitude of the field was measured along the three Cartesian axes, where the zero point is the geometric center point between the pole shoes of the EMBr. Those measurements were performed with a Gauss meter that was traversed by a programmed 3D stepper motor. The comparison of our magnetostatic simulation with the experimental data can be seen in Fig. 4. The almost perfect agreement between both data is impaired by unsymmetrical experimental data which probably were caused by a small misalignment of the stepper motor and the EMBr.

Secondly, we compared the measured excitation field $\mathbf{B}_0$ at the positions of our single coil sensors with the data obtained from the simulation. In the measurements, we observed a slight change in amplitude and phase of the excitation field, depending on the current of the EMBr. Therefore, we ran a simulation with an electromagnetic static solver and a frequency of 1 Hz when only the excitation

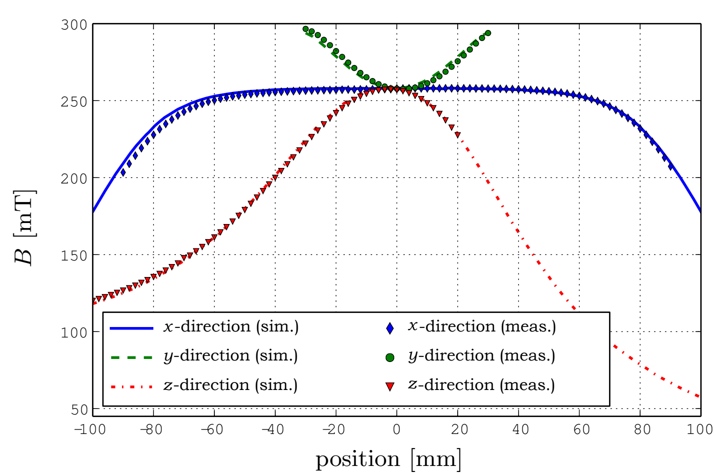


*Fig. 4.* Simulation of the magnetic field amplitude $|\mathbf{B}_{\mathrm{EMBr}}|$ between the pole shoes and comparison with experimental data. The brake-current $I_{\mathrm{EMBr}}$ was 105 A.

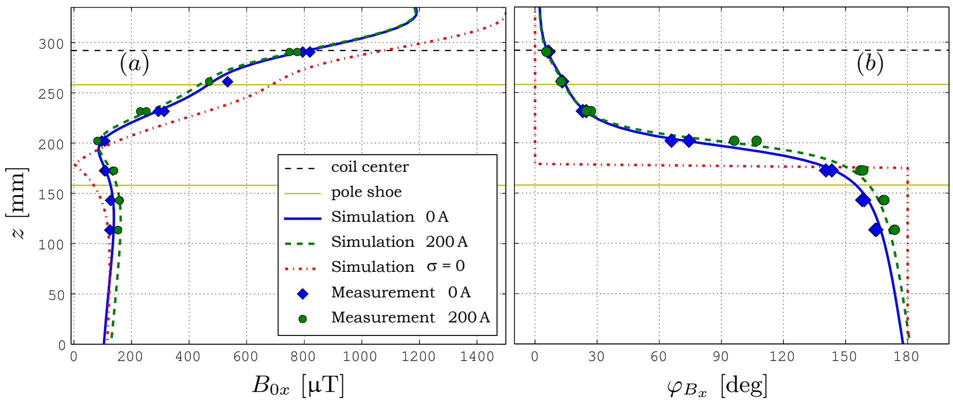


*Fig. 5.* Amplitude ($a$) and phase ($b$) of the $x$-component of the excitation field $\mathbf{B}_0$ along the narrow face of the mould measured with the 340k-pickup-coil and compared to the simulation data. The distance from the center point of the coil-windings to the mould wall was 36 mm.

field was switched on, and another simulation with a transient solver for the case of both fields switched on. The results for both amplitude and phase of $\mathbf{B}_0$ are shown in Fig. 5. Again we find a good agreement between experimental and numerical data. For every sensor position there are two data points (one for each side of the mould). The positions of the pole shoes and the excitation coil are also plotted.

In the right subplot, showing the phase of $\mathbf{B}_0$, one can see a smooth transition between the phase $\varphi = 0$ deg and $\varphi = 180$ deg. This occurs because we have an EMBr with high electrical conductivity and a nonlinear permeability $\mu_r \gg 1$. If one of these properties were missing, then the abrupt phase jump would have been measured. To compare both cases, we added the simulation data, where the pole shoes had zero conductivity and the brake was switched off.

**4. Numerical CIFT experiments.** Now we want to examine how precisely the mould flow can be reconstructed with CIFT for different applied $\mathbf{B}_0$, arising from different experimental setups. We are able to run the experiments with low excitation field frequencies $f \geq 1$ Hz and with different brake currents $I_{\mathrm{EMBr}}$, hence, we must verify in a first step that the choice of $f$ and $I_{\mathrm{EMBr}}$ does not lead to different structures of $\mathbf{B}_0$ that would affect the flow reconstruction. We simulated the $\mathbf{B}_0$ for different cases and compared them to the $\mathbf{B}_0^{\mathrm{ref}}$ obtained for the case of $f = 1$ Hz and $I_{\mathrm{EMBr}} = 0$ A using the measures of correlation

$$\mathrm{Corr}(\mathbf{B}_0, \mathbf{B}_0^{\mathrm{ref}}) = \frac{\mathbf{B}_0 \cdot \mathbf{B}_0^{\mathrm{ref}}}{|\mathbf{B}_0| \cdot |\mathbf{B}_0^{\mathrm{ref}}|} \tag{5}$$

and the mean squared error

$$\mathrm{Err}\left(\mathbf{B}_0, \mathbf{B}_0^{\mathrm{ref}}\right) = \frac{|\mathbf{B}_0 - \mathbf{B}_0^{\mathrm{ref}}|^2}{|\mathbf{B}_0|^2}, \tag{6}$$

where $|\cdot|$ denotes the Euclidean norm.

The results from this comparison can be found in Table 1. It can be easily seen that neither the choice of $f$ nor of $I$ severely affects the spatial structure of $\mathbf{B}_0$. The largest deviation from the reference was obtained for the largest frequency. There are two reasons for this. Firstly, the eddy currents have a larger contribution to the magnetic field at higher frequencies according to the Faraday's law. Secondly,

*Table 1.* Correlation and error for different cases compared with $f = 1\,\text{Hz}$, $I_{\text{EMBr}} = 0\,\text{A}$. Correlations of the $y$- and $z$-component were omitted since for all cases $\text{Corr}_y > 0.9999$ and $\text{Corr}_z = 1.0$.

| $f$ [Hz] | $I_{\text{EMBr}}$ [A] | $\text{Corr}_x$ | $\text{Err}_x$ | $\text{Err}_y$ | $\text{Err}_z$ |
|---|---|---|---|---|---|
| 0 | 0 | 0.99992 | $1.145 \cdot 10^{-3}$ | $3.878 \cdot 10^{-3}$ | $2.819 \cdot 10^{-3}$ |
| 1 | 200 | 0.99999 | $1.873 \cdot 10^{-3}$ | $2.418 \cdot 10^{-4}$ | $9.615 \cdot 10^{-5}$ |
| 3 | 0 | 0.99998 | $2.352 \cdot 10^{-3}$ | $6.926 \cdot 10^{-4}$ | $3.063 \cdot 10^{-4}$ |
| 3 | 200 | 0.99990 | $6.126 \cdot 10^{-3}$ | $9.896 \cdot 10^{-4}$ | $5.312 \cdot 10^{-4}$ |
| 7 | 0 | 0.99981 | $1.194 \cdot 10^{-2}$ | $3.444 \cdot 10^{-3}$ | $1.517 \cdot 10^{-3}$ |

the eddy currents are simulated less accurately because higher frequencies confine the currents to the outer parts of the surface, so the model is less suited for higher frequencies. Creating a well-suited mesh to resolve the induced currents correctly is not easy because of the large dimensions of the model and the small skin-depth

$$\delta = \sqrt{\frac{2}{\sigma\omega\mu_r\mu_0}}, \tag{7}$$

which becomes $\delta = 3.6\,\text{mm}$ for $\omega = 2\pi \cdot 1\,\text{Hz}$, $\mu_r = 1000$ and $\sigma = \sigma_{\text{St37}}$. From this we can say that the choice of $f$ and $I_{\text{EMBr}}$ does not affect $\mathbf{B}_0$ much and, therefore, we can neglect the different cases for the excitation field.

To investigate the reconstruction behaviour of CIFT for actual measurement configurations, we first consider two different cases: a rectangular excitation coil around the mould with the flow creating a mainly $z$-directed $\mathbf{B}_0$ with no EMBr, and a rectangular coil above the pole shoes of the EMBr. The first case is closely related to previous measurements [12] and suites as a reference to see how precisely the flow can be reconstructed.

We started with an OpenFOAM-simulated 3D flow in our model mould for a steady-state. The simulation data were taken from [12]. Since the flow in a slab-casting mould is mainly two-dimensional, the solution was reduced to a 2D flow. The resulting flow is shown in Fig. 6a. In the next step, we solved the forward problem and the inverse problem for the rectangular coil with no EMBr, utilizing

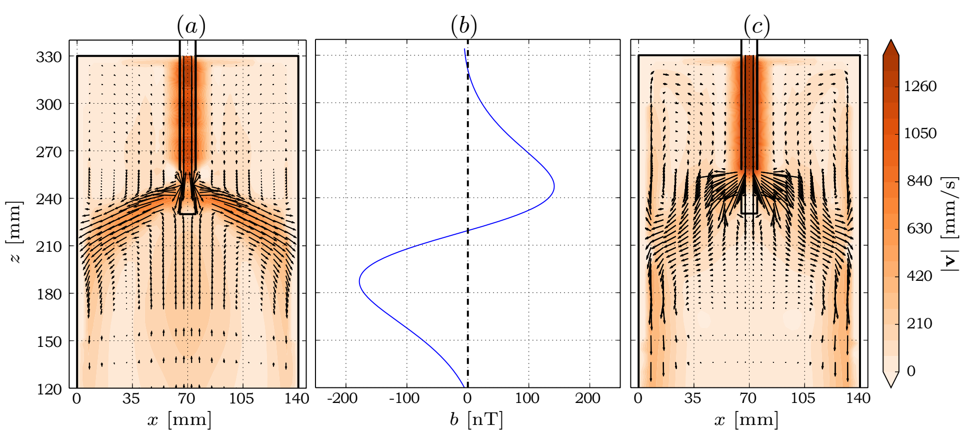


*Fig. 6.* The simulated flow in the mould reduced to the two-dimensional grid used to solve the forward problem $(a)$, the $x$-component of the induced magnetic field $\mathbf{b}$ along the narrow face of the mould for the case of a rectangular coil at $y = 226\,\text{mm}$ with EMBr not present $(b)$, and reconstructed flow pattern $(c)$ from the induced magnetic field.

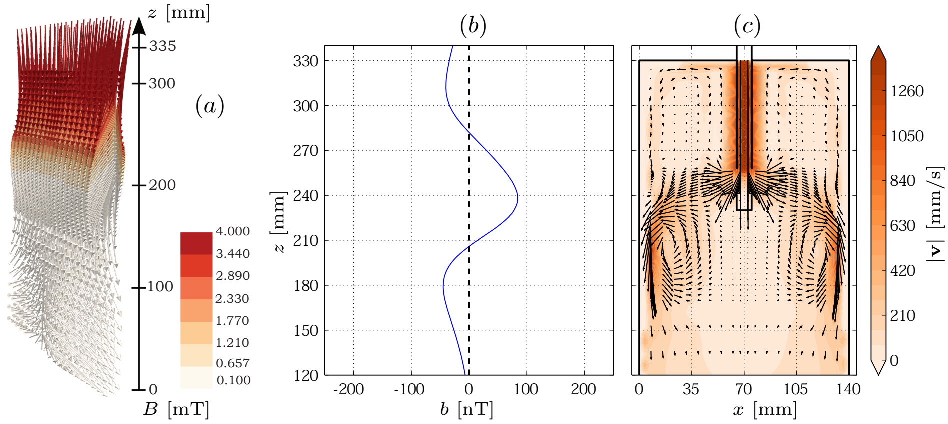


*Fig. 7.* Spatial distribution of $\mathbf{B}_0$ in the mould for the case of one excitation coil above the pole shoes ($a$), induced magnetic field for the applied $\mathbf{B}_0$ ($b$), and reconstructed flow pattern ($c$).

$2 \times 335$ virtual sensors, equally spaced along the center $z$-axis of both narrow faces. The induced magnetic field from the forward problem and the reconstructed flow from the inverse problem can be seen in Fig. 6$b$,$c$. While it is obvious that the exact flow cannot be reconstructed with CIFT, all important flow properties are visible in Fig. 6$c$, that is: the impingement point of the jet on the wall at roughly $z = 210$ mm, the double roll flow pattern, and the outlet angle of the jet. The widened and curved jet is an artifact and results from the regularization [12].

Next we consider one rectangular coil above the EMBr, which is the case related to our experiments (Figs. 3 and 5). The spatial structure of the excitation field, the induced field and the reconstructed velocity are shown in Fig. 7. Fig. 7$a$ makes the effect of the ferromagnetic pole shoes visible. The usually downward directed magnetic flux is pulled out of the mould by the EMBr at a height

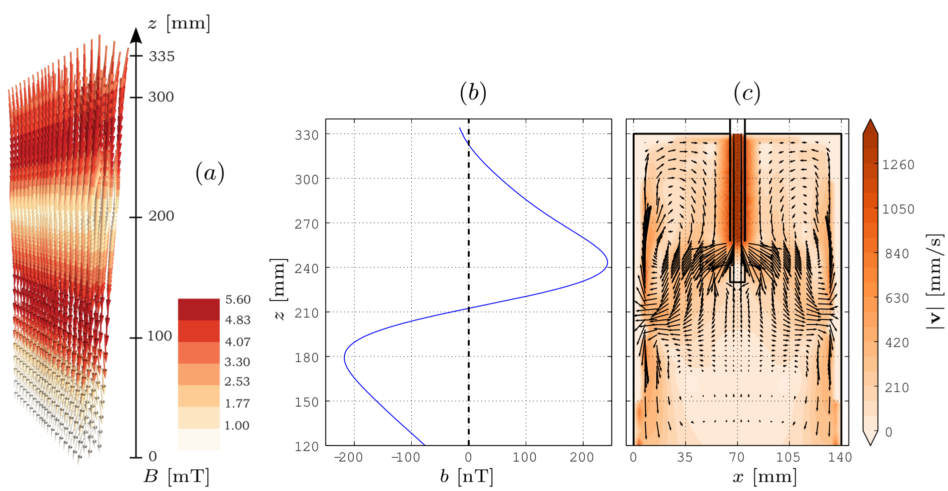


*Fig. 8.* Spatial distribution of $\mathbf{B}_0$ for the case of two excitation coils, one above and one under the pole shoes ($a$), induced magnetic field ($b$), and reconstructed flow pattern ($c$).

$170\,\mathrm{mm} < z < 240\,\mathrm{mm}$. In addition, there is a sudden jump in amplitude of the field at approx. $z = 240\,\mathrm{mm}$, leading to almost no magnetic field in the lower part of the mould. This results in major differences of the induced field compared to the case with no EMBr: the amplitude of $\mathbf{b}$ is also decreased and the graph shows another sign change. One might conjecture that these changes do not affect the reconstruction, since the structure of $\mathbf{b}$ and $\mathbf{B}_0$ is evaluated by the inverse problem solver. This is unfortunately not true, at least for the case of only one applied $\mathbf{B}_0$. Fig. 7c shows that none of the important flow properties were reconstructed. The upper roll shows the increased velocity near the meniscus and has reversed its flow direction, the impingement point moved upwards to $z \approx 240\,\mathrm{mm}$, the jet leaves the SEN almost horizontally and an additional roll is introduced just below the jet. Note that the changed $\mathbf{B}_0$ structure has resulted in an upward shift of the reconstructed flow. One can see that a valid flow reconstruction is not possible with the experiments we did.

Since $\mathbf{B}_0$ with too small amplitudes in the lower part results in wrong features of the reconstructed flow, we considered a third case, where we simulated a setup with an additional coil just below the pole shoes to make sure that the amplitude of the excitation field is large enough throughout the mould. The corresponding results are shown in Fig. 8. The excitation field is now more downward directed and the spatial changes in its amplitude are smaller throughout the entire mould. The induced magnetic field has become more similar to that from Fig. 6, but shows an increased amplitude since the amplitude of $\mathbf{B}_0$ has also increased to roughly 4 mT. In the reconstructed flow, one can see again all the important properties, although the jet is more curved and the flow velocity is increased in the upper part of the mould, especially close to the side walls. Yet the reconstructed flow is sufficiently precise for our application.

**5. Conclusions.** In this paper, we showed that the flow in the mould could be reconstructed by CIFT in the presence of an EMBr if a sufficiently large amplitude of the applied magnetic field throughout the mould is established. This can be achieved by, for example, the use of multiple excitation coils around the mould, possibly above and below the ferromagnetic pole shoes of the EMBr.

The measurement of the induced magnetic field is possible when the EMBr is present in the setup and switched on. Flow reconstructions from experimental data and a comparison with the data obtained from UDV measurements is a subject of ongoing research.

**Acknowledgements.**
This work is supported by Helmholtz-Gemeinschaft Deutscher Forschungszentren (HGF) in frame of the Helmholtz-Alliance LIMTECH. We thank Klaus Timmel and Konrad Klotsche for technical support.

## REFERENCES

[1] World Steel Association. *World Steel in Figures 2013*. http://www.worldsteel.org/

[2] P.H. Dauby. Continuous casting: make better steel and more of it. *Revue de Metallurgie*, vol. 109 (2012), pp. 113–136.

[3] K. Cukierski and B.G. Thomas. Flow control with local electromagnetic braking in continuous casting of steel slabs. *Metallurgical and Materials Transactions B*, vol. 39B (2008), pp. 94–107.

[4] P. Gardin, J.-M. Galpin, M.-C. Regnier *et al.* Influence of electromagnetic brake on molten steel flow and inclusion behavior in a continuous casting mold. *Magnetohydrodynamics*, vol. 32 (1996), no. 2, pp. 189–195.

[5] B.G. Thomas, Q. Yuan, S. Sivaramakrishnan *et al.* Comparison of four methods to evaluate fluid velocities in a continuous slab casting mold. *ISIJ International*, vol. 41 (2001), pp. 1262–1271.

[6] F. Stefani and G. Gerbeth. On the uniqueness of velocity reconstruction in conducting fluids from measurements of induced electromagnetic fields. *Inverse Problems*, vol. 16 (2000), pp. 1–9.

[7] F. Stefani, T. Gundrum, and G. Gerbeth. Contactless inductive flow tomography. *Physical Review E*, vol. 70 (2004), 056306.

[8] T. Wondrak, F. Stefani, T. Gundrum, *et al.* Some methodological improvements of the contactless inductive flow tomography. *International Journal of Applied Electromagnetics and Mechanics*, vol. 30 (2009), pp. 255–264.

[9] K. Timmel, S. Eckert, G. Gerbeth, *et al.* Experimental modeling of the continuous casting process of steel using low melting point metal alloys – the LIMMCAST program. *ISIJ International*, vol. 50 (2010), pp. 1134–1141.

[10] Y. Plevachuk, V. Sklyarchuk, S. Eckert, *et al.* Thermophysical properties of the liquid Ga-In-Sn eutectic alloy. *Journal of Chemical & Engineering Data*, vol. 59 (2014), pp. 757–763.

[11] K. Timmel, S. Eckert, and G. Gerbeth. Experimental investigation of the flow in a continuous-casting mold under the influence of a transverse, direct current magnetic field. *Metallurgical and Materials Transactions B*, vol. 42 (2011), pp. 68–80.

[12] T. Wondrak, V. Galindo, G. Gerbeth *et al.* Contactless inductive flow tomography for a model of continuous steel casting. *Measurement Science & Technology*, vol. 21 (2010), 045402.

[13] T. Wondrak, S. Eckert, G. Gerbeth *et al.* Combined electromagnetic tomography for determining two-phase flow characteristics in the submerged entry nozzle and in the mold of a continuous casting model. *Metallurgical and Materials Transactions B*, vol. 42 (2011), pp. 1202–1210.

[14] T. Wondrak, S. Eckert, V. Galindo *et al.* Liquid metal experiments with swirling flow submerged entry nozzle. *Ironmaking & Steelmaking*, vol. 39 (2012), pp. 1–9.

[15] R.H.D. Townsend. Fast calculation of the Lomb–Scargle periodogram using graphics processing units. *The Astrophysical Journal Supplement Series*, vol. 191 (2010), pp. 247–253.

Received 16.01.2015